Fluid Dynamics in Pleated Membrane Filter Devices

Jannik Dippel[1], Sebastian Handt[1], Birgit Stute[2], Eric von Lieres[2], Thomas Loewe[1]

[1]Sartorius Stedim Biotech GmbH, August-Spindler-Str. 11, 37079 Göttingen,
[2]Forschungszentrum Jülich GmbH, IBG-1: Biotechnology, Wilhelm-Johnen-Str. 1, 52428 Jülich, Germany

1. Abstract

Fluid flow rate and total throughput are the major controlling parameters to calculate the required size of membrane-based filter equipment for manufacturing of pharmaceuticals. The filtration equipment comprises several resistances to the flow such as pipes, connectors and the filter construction itself. The incorporated membrane is a main factor that determines the flow rate through the filter element. With larger membrane area, its resistance to flow declines and total filter throughput increases. Yet, additional hydrodynamic resistances in the filter device lead to lower flow rates than expected from the hydrodynamic resistances of the membrane. Especially the membrane pleats and the spacer material in-between can cause additional flow restrictions. This study investigates the causes of these pleat resistances in manufacturing scale filters. First, manufacturing scale filter flow rates were metered to quantify the effects of pleat geometry, filtration pressure and liquid viscosity on the pleat resistances. Subsequent computed tomography (CT) scans of filter devices, performed under simulated operating conditions, revealed so far unreported pleat compressions that rise with increasing differential pressure up to 50 % at 1.5 bar. In-plane flow resistances of the nonwoven spacer material between the pleats were determined. Finally, these pleat geometries, measured under pressure, and the in-plane nonwoven resistances were implemented into CFD simulations. The simulations show that reduced fluid flow in the nonwoven due to the compression of the pleats can explain the previously observed hydrodynamic pleat resistances.

Keywords: filter cartridge, membrane filter, nonwoven layer, pleating, fluid dynamics, flow resistance, filtration und pressure

2. Notation/Symbols

Symbol	Description
A	Membrane area in [m^2]
P	Pressure in [Pa]
ΔP	Pressure difference in [Pa]
Q	Flow rate in [m^3/s]
J	Flux in [m^3/(m^2·s)]
R	Absolute hydrodynamic resistance of the filtration setup, filter or the membrane pleats in [m^{-3}]
$R°$	Hydrodynamic membrane resistance normalized to the membrane area in [m^{-1}]
k	Permeability in [m^3/(m^2·s·Pa)]
$k_{in\text{-}plane}$	In-plane permeability of the nonwoven in [m^3/(m^2·s·Pa)]
μ	Fluid viscosity in [Pa·s]
ϵ_0	Porosity of non-compressed nonwoven
ϵ_c	Porosity of compressed nonwoven
d_0	Non-compressed pleat width / double-layer nonwoven thickness without compression [m]
d_c	Compressed pleat width / double-layer nonwoven thickness under compression [m]
r	Fiber radius [m]
l	Length of measurement area in the flow cell in [m]
h	Slit height of the flow cell in [m]
w	Slit width of the flow cell in [m]
β	Coefficients of PLS analysis
R^2	Coefficient of determination
Q^2	Coefficient of prediction
LMH	Alternative unit of flux in [L/(m^2·h)]
TMP	Transmembrane pressure
CT	Computed tomography
PLS	Partial least square
CFD	Computational fluid dynamics
PES	Polyethersulfone

3. Introduction

Pleated filter cartridges are commonly used in large-scale pharmaceutical and biopharmaceutical manufacturing. Media, buffer or final fill sterilizing grade filtration are only some of the relevant fields of this application.[1] Fluid flow rate and total throughput are two important parameters that define the performance of a filtration process. Membrane pleating allows a larger area of the filter media to be packed into one element to increase performance with respect to the above-mentioned parameters. A nonwoven layer is inserted between the membrane pleats, acting as a spacer material to ensure uniform utilization of the membrane area. As the pleat density increases, a larger membrane area can be packed into one filter cartridge. This further enhances the total filter throughput, meaning that more fluid is processed before the filtration must be stopped. Consequently, a lower number of filter elements are required in separation processes.[2] There is growing interest in new pleat designs with higher membrane packing densities from different suppliers, such as TwinPleat, M-Pleat or Ultipleat® to achieve a membrane area of as large as 1 m² per 10” filter cartridge.[2–4] However, though the total filter throughput rises with increasing membrane area, additional resistances to the total fluid flow can arise. In fact, an adverse influence of high pleat density on the fluid flow rate is reported in literature.[4,5] For the filtration of non-fouling solutions like buffers, large-area membrane filters might be detrimental, since the total flow rate per filter element does not exceed the flow rate of standard pleat filter cartridges. For this reason, it is important to analyze additional hydrodynamic resistance caused by the pleat geometry. Moreover, detailed and quantitative understanding of the effects of pleat design on filtration is important for scale-up considerations regarding filter flow and total filter throughput.[6,7] The investigation of the fluid flow in pleated cartridges can help to develop pleat designs that are optimized for either high total throughput or high fluid flow. Brown et al. varied the pleat packing of 1” sterilizing grade filter cartridges and showed by water flow experiments that increasing the pleat density and heights raises the hydrodynamic pleat resistance such that the flow rate of the respective cartridge is considerably lower than that of flat sheet membranes at an equivalent pressure.[2] Similar results are reported by other authors.[8,9] However, no model was developed up to now, to calculate the hydrodynamic resistances in the pleats of sterilizing grade filter elements as a function of the pleat geometry, the materials, applied differential pressure and fluid viscosity.

Computational fluid dynamics (CFD) simulations were performed to further investigate the local flow profile in the pleats. Chen et al. have calculated the optimal pleat densities for rectangular pleated air filters to optimize the flow rate using a finite-element numerical model and validated the model against experimental data from Yu et al.[10,11] Fotovati et al. and Saleh et al. used CFD simulations to calculate the pressure drop of pleated air filters exposed to particle deposition. These simulations help to evaluate the optimal pleat design for a high filter performance regarding the fluid flow and the total throughput.[12,13] However, the comparability to liquid flow is limited, since viscosity and density of the fluids differ.[14] CFD simulations with liquids were performed in literature to gain more profound knowledge about the fluid behavior in a pleated filter devices.[15–18] Wakeman et al. performed CFD simulations of filter cartridges for hydraulic fluids used in aeronautical applications. Possible pleat compressions due to drag exerted by the fluid flowing through the membrane was hypothesized and the simulated results were fitted to the experimental data using a so called “compression factor”.[19,20] Transferability from filters for hydraulic fluids to sterilizing grade filters is limited since those filters do not include nonwovens as drainage layers between the membrane pleats. Hence, further investigations are necessary for a more detailed understanding of the flow through sterilizing grade filter cartridges.

In the biopharmaceutical industry, CFD simulations of such pleated sterilizing grade filter elements can lead to better comprehension of the behavior of complex protein solutions during a filtration process. Velali et al. have achieved good agreement of simulated sterilizing grade filter cartridge flow rates to the corresponding experimental values at pressures below 0.5 bar with errors below 10 %.[21] However, as the pressure increases, simulations overestimated the flow rate of the filter cartridges. Additional effects were assumed to potentially cause increased hydrodynamic pleat resistances at higher operating pressures.

In this study, the pleat resistance of manufacturing scale sterilizing grade filters is investigated as a function of the incorporated membrane area, the membrane type, the applied operating pressure and the fluid viscosity. Compared to previous studies, this work includes a broader variation of the pleat geometry as well as different filtration parameters and fluid viscosities. The results can be used to estimate the flow rate in newly developed filter elements by employing a linear regression model.

To investigate the additional pleat resistances at higher pressures, computed tomography (CT) scans were performed to observe the filter device under operation conditions. They show significant pleat compression in the studied filter cartridges. In addition, flow resistances within the pleated layers were characterized by metering the in-plane permeability of the nonwoven that is used as spacer material between the membrane pleats. The results were implemented into a CFD model to achieve a more accurate liquid flow simulations of pleated filter cartridges.

4. Materials and Methods

4.1 Filter Prototyping and Flow Rate Measurements

Prototype 10” filter cartridges were fabricated with varying pleat densities and pleat geometries, to empirically evaluate the influence of pleat geometry on hydrodynamic pleat resistance in commercial filter cartridges. Double-layer PES membranes were used in all cartridges. Table 1 lists an overview of all prototypes employed in this study. Filter elements with two different double-layer membrane types were examined. Some of the filters comprised a 0.45 µm rated pre-filter and a 0.2 µm rated sterilizing grade end-filter and others contained a 0.8 µm rated pre-filter and a 0.45 µm rated end-filter. Diverse types of nonwoven types were used as spacer materials to vary the pleat density. The use of thinner nonwovens results in higher pleat packing and, hence, in larger membrane area incorporated into one filter cartridge. Additionally, the pleat height and the pleat geometry were varied between the mostly used star-pleat and the TwinPleat geometry. Figure 1 shows an example of the pleat geometry of star-pleat cartridge with 95 and 110 pleats as well as a TwinPleat cartridge. All filters were autoclaved once at 121 °C for 15 min and tested in pre-wetted condition for filter integrity by the diffusion method using a Sartocheck 4 Plus Filter Tester (Sartorius) prior to use in filtration.

Table 1: Overview of the varied nonwoven type, membrane, and pleat geometries of the fabricated 10” filter cartridge prototypes. The TwinPleat geometry comprises two pleat heights as shown in Figure 1.

Prototype	Nonwoven	Membrane rated pore size in µm	Pleat number	Pleat height in mm	Pleat type	Membrane area in m²
1	A	0.45/0.2	69	11.5	Star-pleat	0.38
2	B	0.45/0.2	79	11.5	Star-pleat	0.44
3	C	0.45/0.2	94	11.5	Star-pleat	0.52
4	D	0.45/0.2	107	11.5	Star-pleat	0.59
5	D	0.45/0.2	85	15.6	Star-pleat	0.64
6	E	0.45/0.2	117	11.5	Star-pleat	0.65
7	F	0.45/0.2	125	11.5	Star-pleat	0.69
8	G	0.45/0.2	129	11.5	Star-pleat	0.72
9	D	0.45/0.2	120	8.0/14.0	TwinPleat	0.81
10	F	0.45/0.2	143	8.0/14.0	TwinPleat	0.96
11	B	0.8/0.45	73	11.5	Star-pleat	0.40
12	C	0.8/0.45	98	11.5	Star-pleat	0.54
13	D	0.8/0.45	107	11.5	Star-pleat	0.59
14	D	0.8/0.45	88	15.6	Star-pleat	0.66
15	E	0.8/0.45	120	11.5	Star-pleat	0.65
16	F	0.8/0.45	134	11.5	Star-pleat	0.74
17	G	0.8/0.45	135	11.5	Star-pleat	0.75
18	D	0.8/0.45	118	8.0/14.0	TwinPleat	0.80
19	F	0.8/0.45	142	8.0/14.0	TwinPleat	0.98

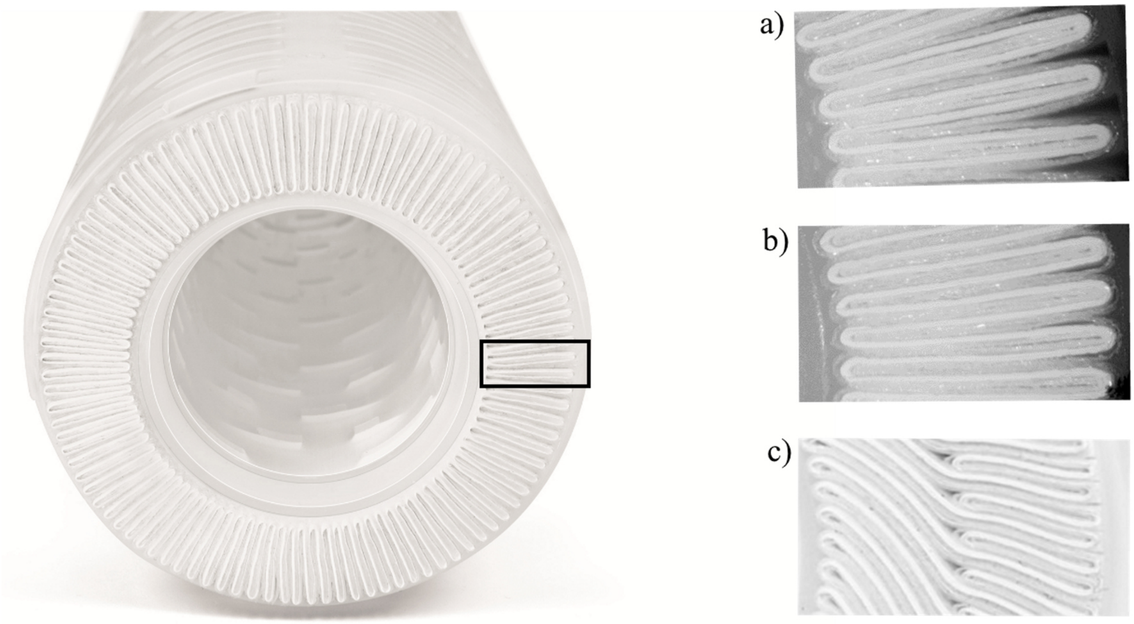

Figure 1: Example cross sections of 10” filter cartridges with different pleat geometries. Star-pleat with *a)* 95 pleats (A = 0.51 m²), *b)* 110 pleats (A = 0.58 m²) and *c)* TwinPleat with 143 full-length pleats (A = 0.96 m²).

Fluid flow measurements were performed with flat disc membrane filters as well as with the filter cartridge prototypes, to calculate the pleat resistance. Membrane production rolls of the cartridge prototypes and the flat disc filters were identical. Fluid flow measurements were performed with water, a 23 wt.% glycerol solution in water (viscosity $\mu = 2$ mPas) and a 41 wt.% glycerol solution in water ($\mu = 4$ mPas). The fluid flow measurements with the water / glycerol solutions were carried out on prototypes 11-19 with incorporated membrane area ranging from 0.38 m² to 0.98 m². The viscosity μ was measured using a Haake™ Mars™ 60 rheometer (ThermoFisher Scientific).

Figure 2 represents the experimental setup of the fluid flow measurements on the flat disc membranes with an effective membrane area of 14.7 cm². In advance, the filters were vented and wetted by water or the respective water / glycerol mixture for 300 s at 0.3 bar pressure. The pressure was measured using a pressure transmitter S-20 (Wika) sensor. Subsequently, the pressure was decreased in steps from 1.5 bar to 0.1 bar, and the flow rate was determined gravimetrically for 120 s using a Quintix 5102-1S balance (Sartorius). The temperature was kept at 20 °C ± 0.2 °C.

The fluid flux J is used for comparison of filter elements with different incorporated membrane area. The fluid flux is defined as the flow rate Q of a filter element normalized to its effective membrane area A.[22] The flux of filters and membranes is typically displayed in the unit L/(min·m²)

$$J = \frac{Q}{A} \tag{1}$$

The filter resistance R is calculated according to Darcy's law (cf. Equation (2)), using the differential pressure ΔP, the fluid viscosity μ and the flow rate Q:

$$R = \frac{\Delta P}{\mu Q} \tag{2}$$

The hydrodynamic resistance $R°_{membrane}$ of the membrane normalized to its EFA is calculated by Equation (3):

$$R°_{membrane} = R_{flat\ disc} A_{flat\ disc} \tag{3}$$

Figure 3 schematically depicts the experimental setup of the fluid flow measurements with the 10" filter cartridge prototypes. The fluid was recirculated in a loop using a rotary pump (Koch). The temperature was maintained at 20 °C ± 0.2 °C using a heat exchanger. A 300 L tank served as a fluid reservoir to ensure constant flow throughout the entire measurement. Before each measurement, each filter cartridge was installed in a stainless steel housing, vented and wetted by the respective fluid for 300 s at a pressure of 0.3 bar. The pressure was recorded using two S-20 pressure transmitters (Wika) and maintained by the automation system, which controls the pump speed. Subsequent to wetting, the pump was adjusted to a fluid flow resulting into a pressure of 1.5 bar, 1.0 bar, 0.5 bar, 0.3 bar, 0.2 bar and 0.1 bar, respectively, between the cartridge inlet and outlet. At each pressure step, the fluid flow rate was recorded for 300 s using a Process master 300 flow meter (Danfos). The pleat resistance was determined by calculating the total filter resistance of the cartridge and subtracting the membrane resistance:

$$R_{pleating} = \frac{\Delta P_{cartridge}}{\mu Q_{cartridge}} - \frac{R°_{membrane}}{A_{cartridge}} \tag{4}$$

The calculated pleat resistance was analyzed as a function of membrane type, fluid viscosity, pressure and membrane area that was built into the studied filter cartridge. The incorporated membrane area of the 10" cartridge was used as quantifiable parameter for the pleat density.

The pleat resistance data were evaluated with Umetrics MODDE Pro 12 (Sartorius Stedim Data Analytics) using a partial least squares regression (PLS) model. This empirical approach allowed to analyze the impact on the pleat resistance of the parameters pressure, fluid viscosity and incorporated membrane area as well as possible interactions of these parameters. Furthermore, this PLS model was used in order to interpolate the pleat resistance for further scale-up considerations. Model quality was evaluated by the coefficient of determination (R^2) and the coefficient of prediction (Q^2).

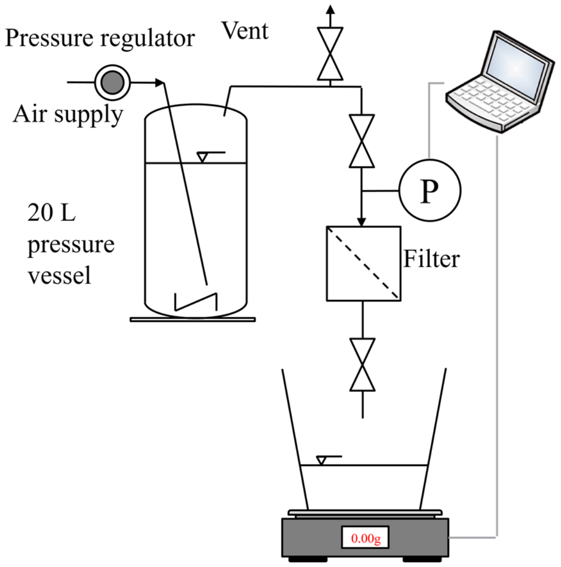

Figure 2: Schematic diagram of the experimental setup for flow measurement of flat disc filters.

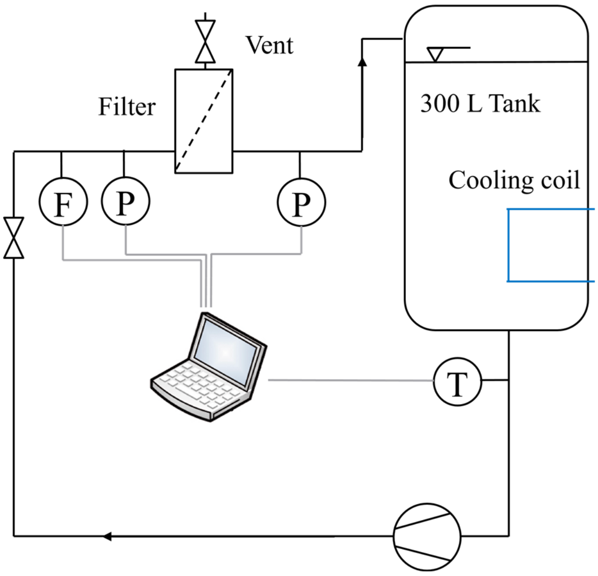

Figure 3: Schematic diagram of the experimental setup to determine the flow rate of 10” filter cartridge prototypes.

4.2 In-plane Flow Measurement in Nonwovens

The fluid permeability of nonwovens depends the flow orientation due to their anisotropic fiber orientation. The in-plane permeability is lower than the permeability in through-plane direction.[23] In a filter cartridge, the fluid flows through the nonwoven in-plane to the fiber orientation. As described by Velali et al., a flow cell has previously been constructed to measure the in-plane nonwoven permeability $k_{in\text{-}plane}$ (cf. Figure 4).[21] A rectangular slit with an adjustable height between h_{slit} = 400 and h_{slit} = 800 µm was positioned between two parallel poly(methyl methacrylate) plates. The inlet of the flow cell was connected to a pressurized vessel filled with water. Two pressure indicators (Wika, 0–4 bar) were placed at positions P_1 and P_2. The differential pressure between them was adjustable. The path length between the two pressure sensors was l = 0.15 m. The width of the slit was w = 0.125 m. The borders were sealed with silicone.

Permeability measurements were performed with the nonwoven types D and E as double, triple and quadruple layers. Each experiment was performed in triplicate with different nonwoven samples. The water flow rate was measured gravimetrically at pressures of 0.2, 0.5, 0.8 and 1.0 bar for 120 s using a Quintix 5102-1S balance (Sartorius) at a temperature of 20 °C ± 0.2 °C. Using the flow rate data, the permeability of the nonwoven through which each sample flowed was determined according to Equation (5).

$$k = \frac{Q\mu l}{\Delta P h_{slit} w} \tag{5}$$

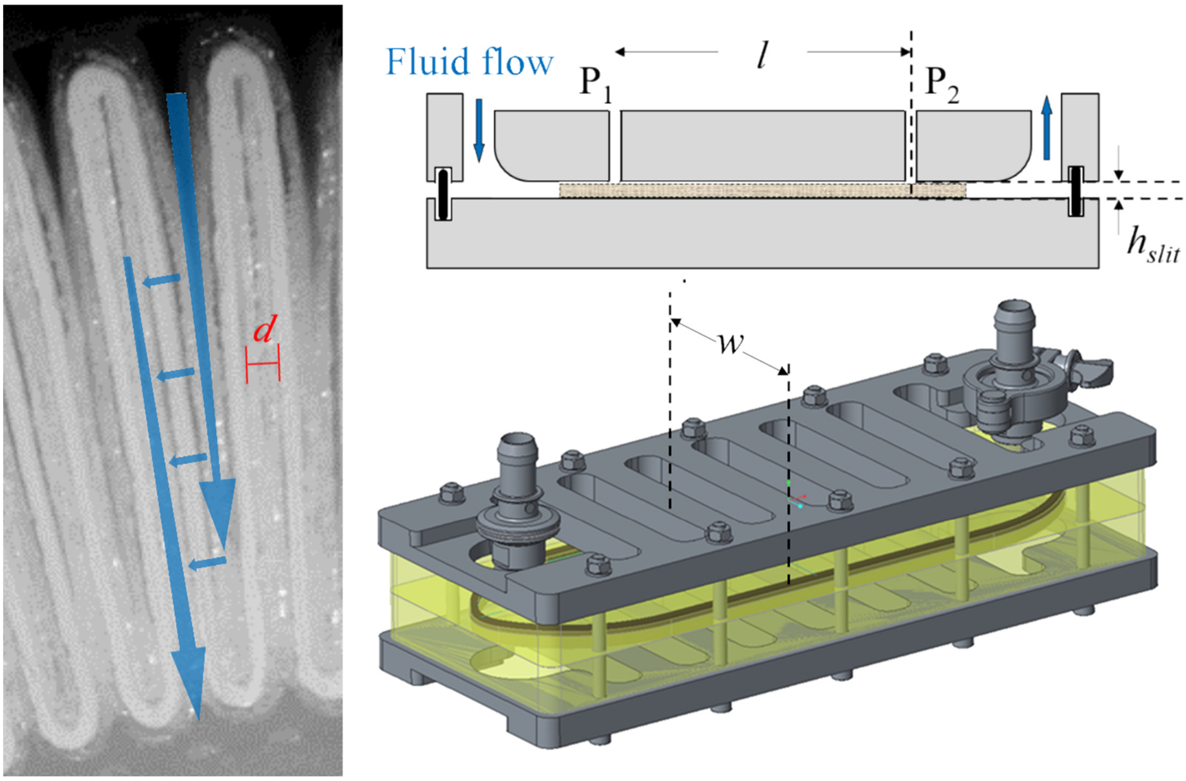

Figure 4: The left image shows schematically an example fluid flow path through a pleated filter cartridge. The fluid flow through the nonwoven is in in-plane direction. An example pleat width *d* at the downstream side is indicated. The right side shows a schematic representation of the experimental setup to simulate the flow through the nonwoven in a filter cartridge. (Edited from Velali et al.[21])

4.3 Computed Tomography Scans of Pleated Filter Cartridges with Applied Transmembrane Pressure

In order to quantify the pleat compressions in filter cartridges, CT scans of filter prototype 4 (equivalent to the commercial Sartopore® 2 0.2 µm 10” MaxiCaps® manufactured by Sartorius), prototype 10 and Millipore Express® SHC High Area were performed, respectively. Before the CT measurements, the filter elements were wetted, and water flow measurements were performed as described above. CT scans of each filter element were taken using a Phoenix® micro-CT scanner (General Electric). The filter capsules’ inlet was connected to a pressurized vessel and air pressure was applied. Using an inlet pressure below the bubble point (3.2 bar) prevents air from passing through the membrane. Consequently, this results in a transmembrane pressure (TMP) that simulates the TMP occurring during a filtration run. The pressurized filter was placed in the measurement area and scanned. Subsequently, the TMP was decreased and the CT scans were performed at each pressure step. The data were evaluated using VGSTUDIO MAX (Volume Graphics GmbH). The pleat width on the upstream and downstream sides of the filter capsule at half pleat height was determined using ImageJ (National Institutes of Health).

4.4 Determination of Compressive Properties of Nonwovens

Pleat compressions in filter cartridges were correlated to mechanical properties of the nonwovens by performing compression experiments. A so-called “Universal Testing Machine”, Inspect Duo (Hegewald & Peschke), was used. Ten samples from three lot numbers of the nonwovens, types D and F, were prepared and measured in double-layer circular discs with an area of 17.3 cm². The thickness of each sample was measured in advance using a micrometer screw. Subsequently, the samples were placed between two round plates with an area of 17.3 cm² and compressed up to a pressure of 2 bar (347 N). The compressive properties of the nonwoven were correlated to the pleat width *d* under pressure.

4.5 Computational Fluid Dynamics (CFD) Simulation of Pleated Filter Devices Under Pressure

COMSOL Multiphysics 5.5 was used to perform finite element CFD simulations. Previous studies have shown a negligible effect of the plastic cage on the total fluid flow across sterilizing grade filter cartridges.[21] Hence, three-dimensional modeling of the cartridge does not lead to increased accuracy of the simulated fluid flow. Consequently, the simulations in this work were performed with a two-dimensional cross section model of the pleats. Geometries of pleat cross sections at different degrees of pleat compressions were manually reconstructed from the CT scans using Inkscape as described by Velali et al.[21] Additionally, generic single pleat models were constructed, including the different pleat compressions. Symmetry conditions were applied at the side boundaries of these single pleat models to represent the whole cross section of the filter cartridge. These geometries were imported to COMSOL Multiphysics 5.5 and partitioned into several domains with different physical properties. Figure 5 provides an overview of the pleat modelling approaches and shows the different domains in the generic pleat models and in the manually reconstructed pleat models. The void domains at the upstream and the downstream sides of the filter were described by Naiver-Stokes equations.

$$\rho(\upsilon * \nabla)\upsilon = -\nabla p + \nabla(\mu(\nabla\upsilon + (\nabla\upsilon)^T) \tag{6}$$

$$\rho\nabla\upsilon = 0 \tag{7}$$

The porous domains with membrane or nonwoven materials were described by Brinkman equations.

$$\rho\left(\frac{\upsilon}{\epsilon} * \nabla\right)\frac{\upsilon}{\varepsilon} = -\nabla p + \nabla(\mu\left(\nabla\frac{\upsilon}{\epsilon} + \left(\nabla\frac{\upsilon}{\epsilon}\right)^T\right) - \frac{\mu}{\kappa}\frac{\upsilon}{\varepsilon} \tag{8}$$

$$\rho\nabla\frac{\upsilon}{\varepsilon} = 0 \tag{9}$$

Here, υ is the liquid velocity, p the local pressure, $\rho = 1000\frac{kg}{m^3}$ the liquid density, $\mu = 0.001\ Pa \cdot s$ the dynamic viscosity, ε the porosity and κ the permeability of the porous region.

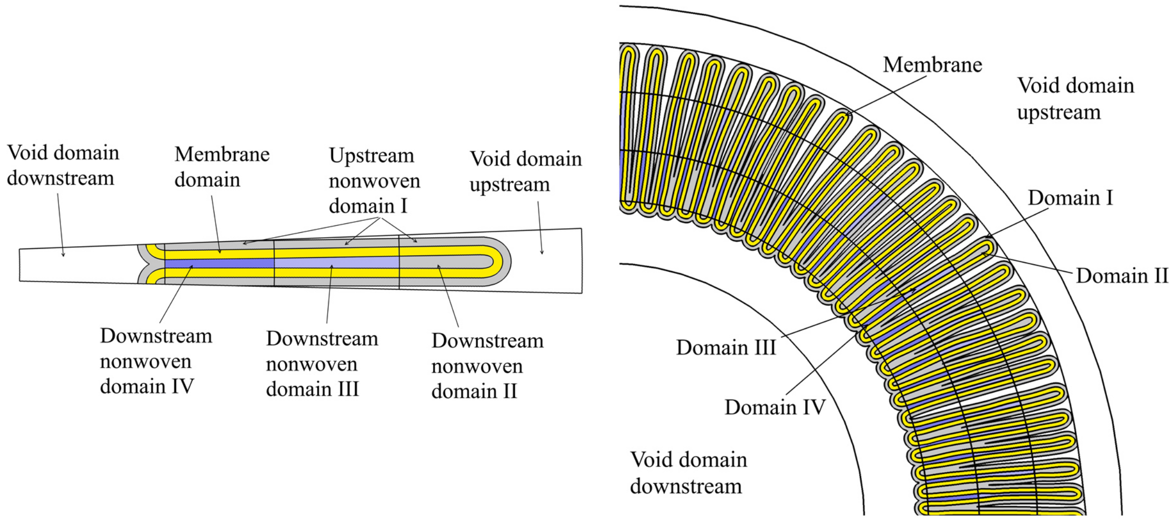

Figure 5: Schematic representation of example model geometries. Generic single pleat model (*left*) and from CT scans reconstructed pleat model (*right).* The white areas are void domains at the upstream and downstream of the filter cartridge. The membrane domain is indicated yellow. Domain I represents the nonwoven at the upstream side. Domains II, III and IV represent the nonwoven at the downstream side at different degrees of compressions. The permeability and porosity of each domain is reported in Table 2.

The permeability of the membrane was obtained from experiments described in section 4.1. The permeability of the nonwoven on the upstream side was obtained from experiments described in section 4.2. To consider the compression on the downstream side of the pleats, the nonwoven was split in up to three domains. This represents a discretization of the continuous compression increase into three domains with constant properties. The compression of the nonwoven on the downstream side, results in a reduced permeability and porosity. Hence, the permeability and porosity in each of the three nonwoven domains was adjusted according to its degree of compression. The average compression of the nonwoven in these three regions downstream of the membrane was determined from CT scans measured at the respective pressure drops. Table 2 lists the permeabilities and porosities of the nonwoven domains as a function the applied pressure and the degree of compression. Further details on the calculation of the compressed nonwoven permeability and porosity are described in section 5.2.

Simulations at different degrees of detail were performed with the manual reconstructed pleat model and the generic pleat model to individually analyze the effect of different impact factors on the accuracy of the model prediction. Table 3 depicts an overview of the simulations performed. All simulations without consideration of pleat compressions are based on the pleat model at a differential pressure of 0 bar. The simulations without consideration of reduced nonwoven permeability and porosity used the same material properties of the uncompressed nonwoven on the downstream and on the upstream side.

Table 2: Nonwoven porosity and permeability used in the different nonwoven domains for the CFD simulations at various pressures.

Pressure [bar]	Nonwoven domain	Nonwoven compression	Nonwoven porosity ϵ_c [-]	Nonwoven permeability k [m²]
		Models without nonwoven compression		
all	I-IV	0 %	0.73	2.45×10^{-10}
		Models with nonwoven compression		
0.3	I-II	0 %	0.73	2.45×10^{-10}
	III	15 %	0.68	1.54×10^{-10}
	IV	25 %	0.64	1.04×10^{-10}
0.5	I-II	0 %	0.73	2.45×10^{-10}
	III	20 %	0.66	1.28×10^{-10}
	IV	35 %	0.59	6.30×10^{-11}
1.0	I-II	0 %	0.73	2.45×10^{-10}
	III	25 %	0.64	1.04×10^{-10}
	IV	44 %	0.52	3.60×10^{-11}
1.5	I-II	0 %	0.73	2.45×10^{-10}
	III	37 %	0.60	6.00×10^{-11}
	IV	47 %	0.49	2.90×10^{-11}

All geometries were meshed using the COMSOL setting “fine for fluid dynamics” with automated mesh refinement. In a mesh independence study, further mesh refinement was observed to yield practically the same results (data not shown). Stationary solutions of the equations (6) to (9) were computed at different pressure drops across the outer boundaries of the respective geometry. The average linear velocity in m/s was determined at the outer domain boundary and multiplied by the circumference (223 mm) and height (239 mm) of the cartridge to compute the volumetric flow rate in L/min for comparison with experimental measurement data.

Table 3: Overview and nomenclature of the performed CFD simulations with different degrees of detail.

Simulation	Pleat geometry modeling	Consideration of pleat compression	Consideration of reduced porosity and permeability of nonwoven due to pleat compression
1a	Reconstruction via image analysis from CT scans	No	No
1b	Generic single pleat design	No	No
2a	Reconstruction via image analysis from CT scans	Yes	No
2b	Generic single pleat design	Yes	No
3a	Reconstruction via image analysis from CT scans	Yes	Yes
3b	Generic single pleat design	Yes	Yes

5. Results and Discussion

5.1 Experimental Determination of Pleat Resistance

In order to investigate the hydrodynamic pleat resistances of manufacturing scale sterilizing grade filter, flow rate measurements were performed with filters comprising different pleat geometries, membrane and nonwoven types, using various fluid viscosities and operating pressures. The hydrodynamic pleat resistances were calculated using Darcy's law, subtracting the membrane resistance. A partial least squares regression (PLS) analysis was performed to determine the major factors that impact the fluid flow rate.

The fluid flux J is used to compare filter elements with different incorporated membrane areas. It is defined as the total filter flow rate Q across the filter normalized to the effective membrane area A (cf. Equation (1)). Figure 6 depicts the flux J of three sample prototypes (1, 4 and 10) with a membrane area of 0.39 m², 0.59 m² and 0.96 m², as well as the flux through a flat disc of the same membrane type versus the applied pressure. As the incorporated membrane area per 10" filter cartridge increases, the pleat packing density rises and the flux declines. This indicates additional hydrodynamic resistance due to the membrane pleats. Brown et al. have shown that additional pleat resistance become higher as the pleat packing density and the pleat height in a 1" sterilizing grade filter increases. They also measured a significant reduction in the flux for 10" cartridges compared with flat discs.[2]

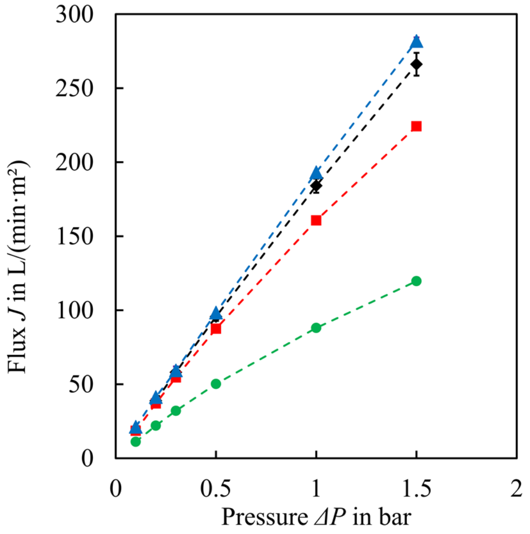

Figure 6: Water flux J of flat disc membrane (blue ▲) and 10" filter cartridge prototypes: Prototype 1 with 0.39 m² membrane area (black ♦); prototype 4 with 0.59 m² membrane area (red ■); prototype 10 with 0.96 m² membrane area (green •). Lines serve as visual guidance. Error bars represent standard deviations. (n=3)

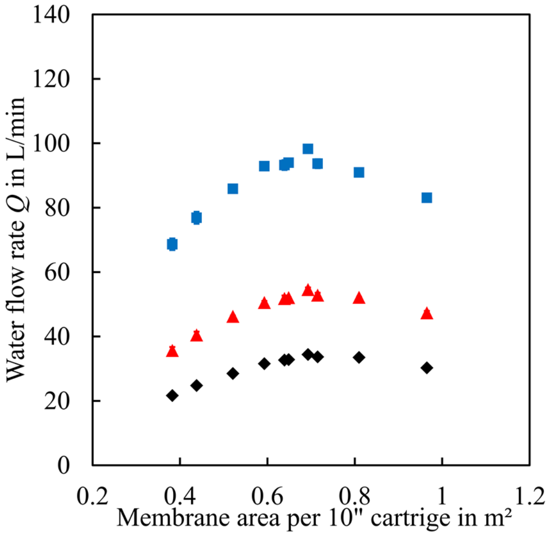

Figure 7: Total water flow rate Q of the Sartopore 2 0.2 µm 10" cartridge versus incorporated membrane area at a pressure of 0.3 bar (black ♦), 0.5 bar (red ▲) and 1.0 bar (blue ■). Error bars represent standard deviations. (n=3)

The membrane area incorporated per 10” filter cartridge is used as a quantifiable parameter that describes the pleat packing density. A higher pleat packing density can be achieved by using a thinner nonwoven as spacers material, larger pleat heights, or a more compact pleat geometry, such as TwinPleat. Figure 7 depicts the water flow rate versus the incorporated membrane area for the filter cartridges with 0.45/0.20 µm membranes at 0.3, 0.5 and 1.0 bar. The flow rate rises with increasing membrane area packed per 10” cartridge up to a maximum, in this case 0.7 m². Beyond this maximum, where the membrane area and, consequently, the pleat packing density causes diminished accessibility of the membrane pleats and decreased filter flow rate as a result. Hence, an optimal filter density, that is a pleat packing density for maximum filter flow rate, can be found. Yet the optimal pleat packing density depends on the normalized membrane resistance $R°$. In other words, depending on the membrane type, the optimum can change. More permeable membrane types shift the optimal pleat packing density towards lower values.

The hydrodynamic pleat resistance is calculated by determining the total resistance of the 10” filter cartridge according to Darcy’s law and subtracting the membrane resistance (cf. Equation (4)). Figure 8 shows an example of the pleat resistance of prototypes 1-10 in water flow experiments versus the incorporated membrane area and the applied pressure. As expected, the pleat resistance rises as the membrane area incorporated per filter cartridge increases. Furthermore, higher apparent pleat resistances are measured at increased flow rates. With an incorporated membrane area of 0.38 m² and an applied pressure of 0.2 bar, the pleat resistance R_{pleat} contributes $0.92 \cdot 10^{10}$ m^{-3}, i.e. less than 3 % to the total filter resistance R_{total} and can therefore be neglected in comparison to the membrane resistance $R_{membrane}$. However, with an incorporated membrane area of 0.96 m² and a pressure of 1.5 bar (corresponds to a flow rate of 110 L/min), the pleat resistance contributes $4.8 \cdot 10^{10}$ m^{-3}, that is as much as 60 % of the total filter resistance.

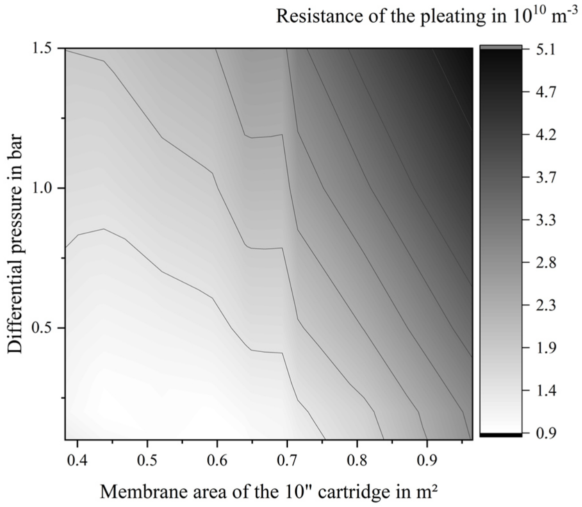

Figure 8: 2D contour plot of the hydrodynamic pleat resistance in 10” filter cartridges versus the incorporated membrane area per filter element and the applied pressure.

A PLS analysis (Section 4.1) of the pleat resistance was performed to fit a mathematical regression model to the measured data and to identify major factors that impact the filter flow rate. The factors tested were membrane type, fluid viscosity, membrane area and applied pressure. The parameters were normalized to non-dimensional variables from -1 to 1 to make the coefficients comparable to each other. A good model was obtained, as indicated, by $R^2 = 0.92$ and $Q^2 = 0.90$,[24] although the high values of R^2 and Q^2 are partially attributed to the large volume of experimental data. Figure 9 shows the coefficient plot of PLS analysis. As expected, the membrane type was found to be insignificant regarding the pleat resistance, since the membrane resistance and the pleat resistance are assumed to contribute additively to the total filter resistance. The incorporated membrane area A had the highest impact on the pleat resistance as this area is related to the pleat packing density. A significant quadratic term $A \cdot A$ is observed, indicating a disproportionate growth in the pleat resistance as the membrane area increases. The membrane area can be varied by changing the incorporated nonwoven material, the pleat height or the pleat geometry.

A significant positive influence of the pressure on the pleat resistance is observed. Pleat resistance grows as the pressure increases. This indicates pleat compressions due to a TMP, causing a lower pleat width d on the downstream side of the filter element. Pleat compressions are described in more detail in Section 5.2. The lower pleat width increases the pleat resistance similarly to a higher pleat packing density. This effect causes the flow rate of pleated filter cartridges to increase disproportionally with respect to the applied pressure, as shown in Figure 8. Consequently, the combination of high differential pressure and high membrane area results in highest pleat resistance. A minor negative influence of viscosity on the pleat resistance is observed. Yet this effect is negligible compared to the impacts of membrane area and applied pressure. However, a strong interaction between viscosity and applied pressure is observed. The negative interaction parameter indicates that at higher viscosities, the impact of pressure on the pleat resistance decreases. The reason for this interaction cannot be explained within the scope of this study and requires further investigation. The flow rate experiments and, therefore, measurements of the pleat resistance were performed with prototypes containing a combination of 0.80/0.45 µm membranes. Since water flow experiments do not show any influence of the membrane type on the pleat resistance, the effect of the fluid viscosity is assumed to be independent of the membrane type as well.

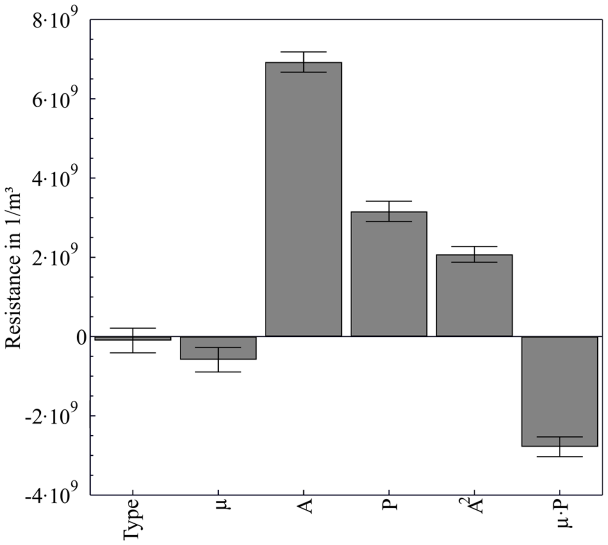

Figure 9: PLS model coefficient plot for the pleat resistance as a response. The parameters are membrane type (type), fluid viscosity (μ), incorporated membrane area (A) and applied pressure (P). The membrane type is a qualitative parameter, whereas the other parameters are quantitative. The quadratic terms for incorporated membrane area ($A*A$) and interaction between viscosity and pressure ($\mu*P$) were identified as significant.

As describe above, the membrane type does not have a significant influence on the pleat resistance. Hence, a linear regression model can be used to describe the resistance as a function of incorporated membrane area, applied pressure and fluid viscosity (Equation (10)) within the investigated range. An extrapolation of the data to larger pressures or fluid viscosities is potentially possible to a limited extend. Table 4 lists the coefficients β that were obtained by fitting the regression model to the experimental data.

$$R_{pleating} = f(A,P) = \beta_0 + \beta_\mu \mu + \beta_A A + \beta_P P + \beta_{AA} A^2 + \beta_{\mu P} \mu P \begin{cases} \mu = 1\,mPas - 4\,mPas \\ A = 0{,}3\,m^2 - 1{,}2\,m^2 \\ P = 0{,}1\,bar - 2\,bar \end{cases} \tag{10}$$

Table 4: Coefficients of the pleat model for sterilizing grade filter prototypes fitted by the PLS approach (cf. Equation (10)).

Model coefficients β	Value	Standard Error
Constant (β_0)	$1.11\cdot10^{10}$	$0.16\cdot10^{9}$
Fluid viscosity (β_μ)	$-0.62\cdot10^{9}$	$0.13\cdot10^{9}$
Membrane area (β_A)	$6.92\cdot10^{9}$	$0.13\cdot10^{9}$
Flow rate (β_P)	$3.18\cdot10^{9}$	$0.13\cdot10^{9}$
Membrane area squared (β_{AA})	$2.05\cdot10^{9}$	$0.10\cdot10^{9}$
Viscosity·flow rate ($\beta_{\mu P}$)	$-2.82\cdot10^{9}$	$0.13\cdot10^{9}$

This empirical model allows to calculate the flow rate of process-scale pleated filter cartridges independent of the incorporated membrane type: 1) Determine the membrane resistance normalized to the membrane area $R°$ using Equations (2) and (3). 2) Determine the incorporated membrane area of the

10” filter cartridge. 3) Add the membrane resistance and the pleat resistance to calculate the filter cartridge flow rate Q according to Darcy’s law using Equation (11).

$$\Delta P = Q\mu\left(R_{membrane} + R_{pleat}\right) = Q\mu\left(\frac{\mathrm{R}^{\circ}}{\mathrm{A}} + R_{pleat}(A, P)\right) \tag{11}$$

The pleat resistance R_{pleat} is calculated using Equation (10) and the empirically determined coefficients β obtained from Table 4.

This model is used to calculate the optimal pleat design with low flow restrictions for various membrane types. Moreover, accurate flow rates are calculated from small scale filtration trials to determine the required filter size in flow rate limited filtration processes. Note that the total filter throughput is not considered in this model. For filtration processes that are limited by the total filter throughput due to membrane fouling, high pleat densities with a large membrane area per filter element are advantageous.

5.2 Pleat Compressions in Filter Cartridges Under Pressure

As described in section 5.1, the increased pleat resistance at higher pressures is hypothesized to be caused by pleat compressions. In this study, CT scans of pleated filter elements with an applied TMP were performed to analyze and quantify pleat compression. Prior to the scans, the hydrophilic PES membranes were wetted to fill the membrane pores with water. During the CT scans, an air pressure below the bubble point of the membrane was applied at the inlet of the filter cartridge. The downstream side of the filter was kept at atmospheric pressure. As long as the applied pressure does not exceed the capillary effects of the membrane pores, a TMP is simulated that is equivalent to the operating pressure during filtration.[25] The TMP difference during filtration is due to the drag exerted by the liquid flowing through the membrane.[26]

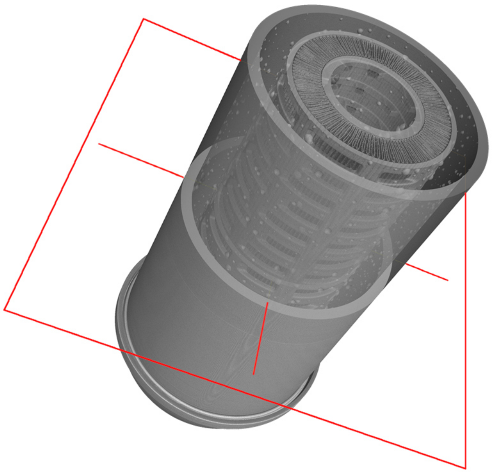

Figure 10: 3D CT scan of prototype 4 of the 10” filter cartridge without TMP applied. The red plane represents the cross section that is used for image analysis to determine the pleat width *d*.

Cross sections of the CT scans were taken at the middle of each filter as shown in Figure 10. Figure 11 depicts details of these cross sections at different TMPs applied. Due to filter symmetry, these cross sections are representative of the whole filter element. For the filter prototype 4 with the star-pleat geometry (equivalent to the commercial Sartopore® 2 0.2 µm filter), symmetrical pleats are observed on both the upstream and downstream sides without TMP applied. At higher TMPs the pleats are compressed toward the downstream side. The pleat width at the downstream side $d_{downstream}$ decreases and the pleat width at the upstream side $d_{upstream}$ increases as the pressure rises. Similar results are observed for high-area pleat geometries, such as the TwinPleat of prototype 10 and the M-Pleat of the Millipore Express® SHC High Area cartridge. As the TMP increases, a compression of the pleats towards the downstream side is observed. For all three cartridges, these pleat compressions were observed over the whole length of the cartridges except for the outer 1 mm after the end caps welds on each side (data now shown).

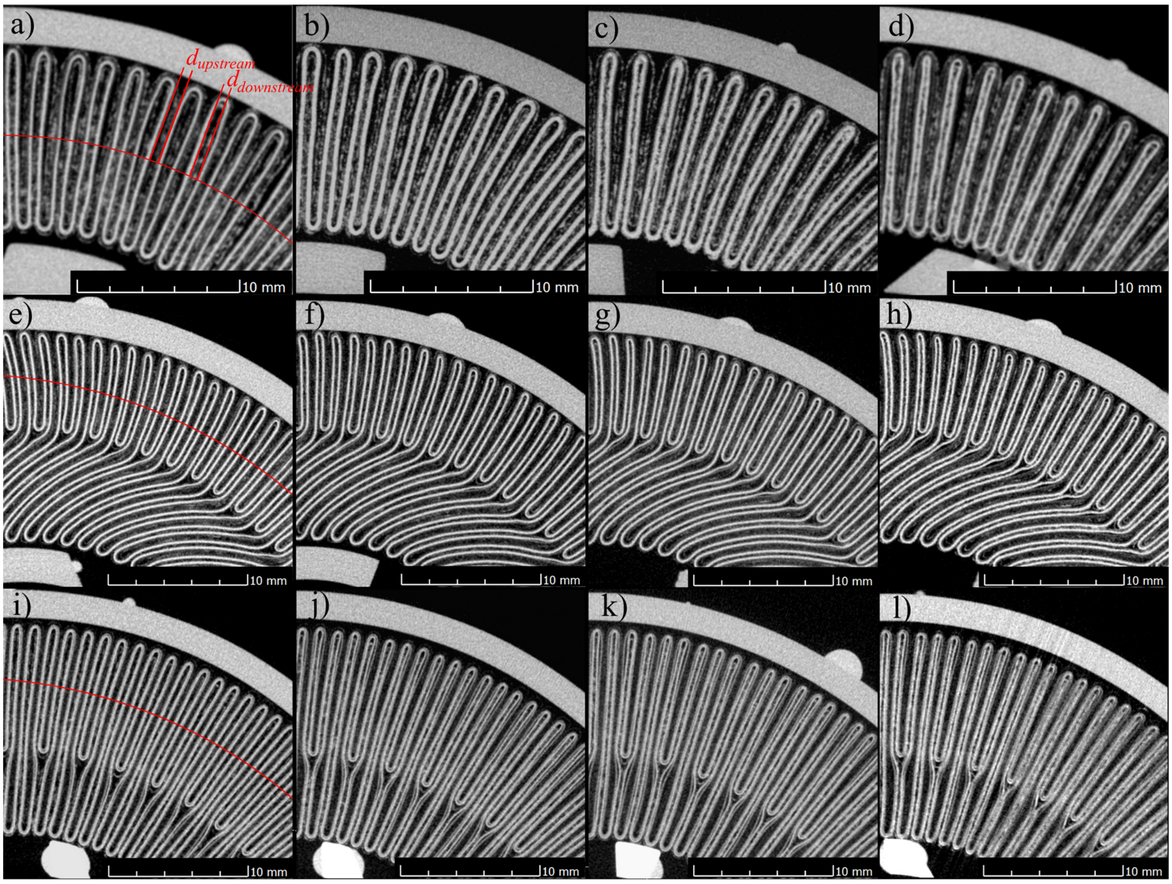

Figure 11: CT scans of 10” filter cartridges. Cross sections of pleats at a TMP of 0.0 bar, 0.5 bar, 1.0 bar and 1.5 bar *(from left to right)* applied to the filter with star-pleat geometry *(a-d)*. Cross sections of the pleats with a TMP of 0.0 bar, 0.5 bar, 1.0 bar and 2.0 bar *(from left to right)* applied to the filters with TwinPleat *(e-h)* and M-Pleat *(i-l)* geometry, respectively. Cross sections of the same filter cartridge at different TMPs were scanned at identical positions. The red curve in images *a*, *e* and *i* represents the position where the pleat width is measured. Example pleat widths at upstream side $d_{upstream}$ and downstream side $d_{downstream}$ are indicated in (*a*).

The pleat compressions under TMP were further quantified and correlated to the mechanical properties of the nonwoven. For this purpose, the pleat widths on the upstream and downstream sides were evaluated graphically at the height of the red curve, respectively (cf. Figure 11).

Additionally, compression experiments of double-layer nonwoven specimens were performed to analyze the thickness of the nonwoven versus the applied pressure. Figure 12 shows the pleat width *d* at the upstream and downstream sides as well as the nonwoven thickness from the compression experiments versus the applied pressure. The pleat width of the star-pleat geometry increases by 27 % at the upstream side from 670 ± 100 µm to 850 ± 160 µm at 1.5 bar. The pleat width on the downstream side decreases by 40 % from 470 ± 100 µm to 190 ± 50 µm. At 2.0 bar, the pleat width on the downstream side of the TwinPleat filter is reduced by 50 % from 270 ± 30 µm to 140 ± 30 µm. At 2.0 bar, the pleat width on the downstream side of the M-Pleat filters also decrease by 50 % from 300 ± 45 µm to 150 ± 35 µm. Hence, the pleat compression of both high-area filter cartridges are equal within standard deviations. Compression experiments of the nonwovens D and F that are entailed in the prototype cartridges 4 and 10 are depicted as a blue line in Figure 12. The compression response of the nonwoven under load correlated with the pleat width at the downstream side. This correlation can be used in the future to estimate pleat compressions in filter elements under pressure with a simple experimental setup of nonwoven compression experiments. By using stiffer nonwovens on the downstream side, the pleat compressions can potentially be reduced.

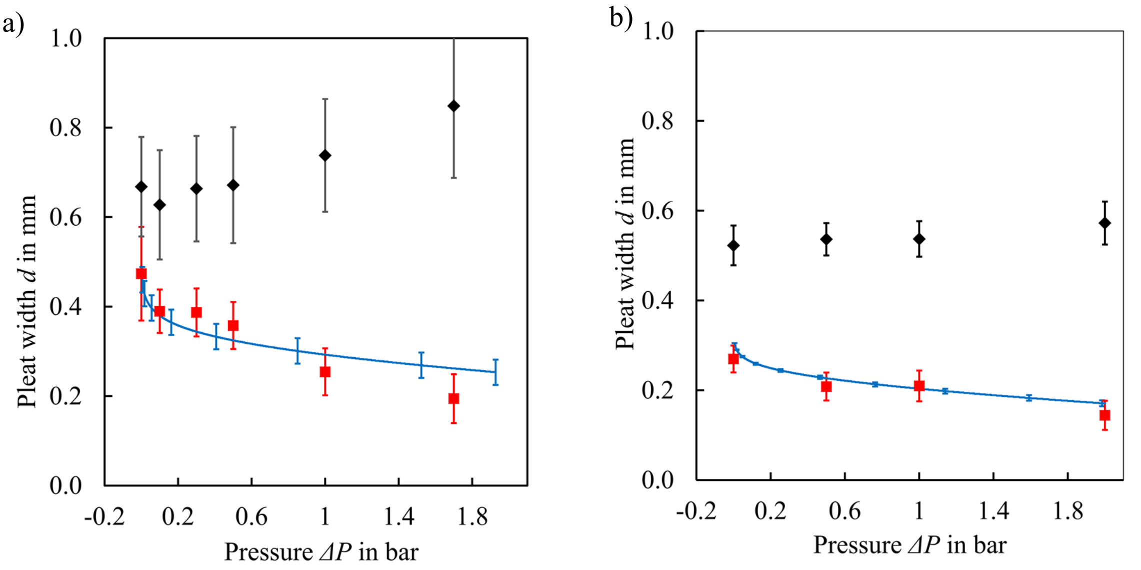

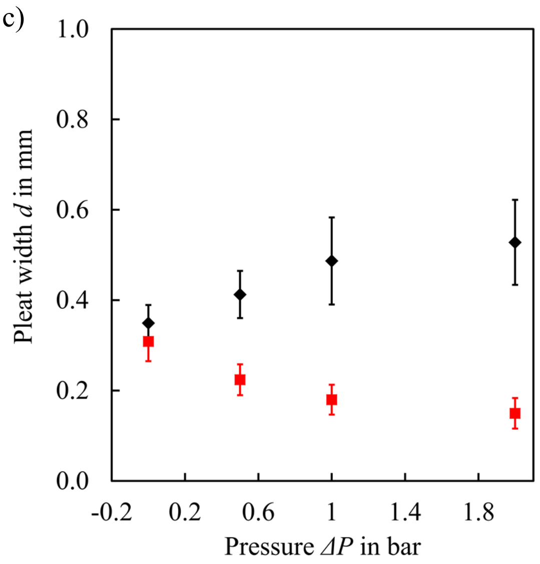

Figure 12: Pleat width of 10” cartridges on the upstream side (black ♦) and the downstream side (red ■) at different TMPs according to CT scans. Pleat width was determined graphically at half the pleat width. Star-pleat geometry of prototype 4 *(a)*; TwinPleat geometry of prototype 10 *(b)* and M-Pleat geometry *(c)*. Error bars represent standard deviations over all pleats. Blue lines show compression of the corresponding double-layer nonwovens D and F obtained in compression experiments. Error bars show standard deviations over ten specimens.

The CT measurements were performed under static conditions with a TMP applied, but without liquid flow. During a filtration run, pulsation of the pump might potentially lead to movement of the pleats. Furthermore, the dynamic pressure of the liquid moving through the pleats might additionally influence the pleat geometry. Yet, as shown by CFD simulations, the local flow rates in the nonwoven between the membrane pleats are relatively low and, therefore, the TMP is assumed to have the major influence on pleat compression.

The compression of the pleats and of the nonwoven at the downstream side, decreases the cavity size between the fibers. This reduces permeability of the nonwoven and therefore the flow of liquid through the pleats. Permeability measurements were performed without compression using a flow cell. Flow measurements of compressed nonwovens used in this study are not feasible due to the large forces that need to be applied in order to achieve significant compression. Hence, a theoretical approach is used to estimate the flow behavior of the nonwovens on the downstream side of the pleats.

The porosity ϵ_0 of the uncompressed nonwoven type D used in this study is 78 %. Equation (12) was used to calculate the porosity ϵ_c of the compressed nonwoven is based on the initial porosity ϵ_0 and the thickness of the compressed nonwoven d_c compared to the initial thickness of the nonwoven d_0:

$$\epsilon_c = 1 - \frac{d_0(1-\epsilon_0)}{d_c} \tag{12}$$

Due to the lower porosity, the cavities between the fibers decrease and the in-plane permeability in the nonwoven decreases. Various analytical and numerical models are proposed to describe the fluid permeability of isotropic and anisotropic fiber webs or nonwovens meshes, since the liquid flow plays an important role in many engineering applications in the textile industry or in various steps of papermaking.[27–30] Lawrence et al. and Håkanson et al. provide an overview on several analytical models that describe the flow through needle-punched nonwovens in through-plane and in-plane direction.[31,32] The nonwovens used in their studies for comparison of different permeability models are thicker than in this study. Nevertheless, the geometric structures of the fibers are similar. Both publications show that the Happel-p model provides a good estimation of the impact of porosity decrease on the decline of fluid permeability in in-plane flow for various nonwoven types. This model assumes parallel linear fibers through which liquid flows across their length. The in-plane liquid permeability of the nonwoven k_n is calculated by Equation (13) using the porosity ϵ and the fiber radius r.

$$k_n = \frac{r^2}{4(1-\epsilon_c)}\left[ln\left(\frac{1}{(1-\epsilon_c)}\right) - \frac{3}{2} + 2(1-\epsilon_c) - \frac{(1-\epsilon_c)^2}{2}\right] \tag{13}$$

Interweaving of the fibers and the resulting tortuosity of the fluid cavities in the nonwoven are neglected in the Happel-p model. Hence, it overestimates the absolute flow rate compared with the experimental results. In order to account for the tortuosity an apparent fiber radius is calculated with Equation (13) using the permeability values from the flow cell measurement without compression. The apparent fiber radius of 28.8 µm is lower than the real fiber radius of the nonwoven due to tortuosity. Using this apparent diameter and Equation (12), the in-plane permeability of compressed nonwovens is calculated from the thickness of the compressed specimen.

$$k_n = \frac{r^2 d_c}{4d_0(1-\epsilon_0)}\left[ln\left(\frac{d_c}{d_0(1-\epsilon_0)}\right) - \frac{3}{2} + \frac{2d_0(1-\epsilon_0)}{d_c} - \frac{d_0^2(1-\epsilon_0)^2}{2d_c^2}\right] \tag{14}$$

In the following section the reduced permeability and porosity of the nonwoven are used as input parameters for CFD simulations to describe their impact on the total fluid flow in sterilizing grade filter cartridges.

5.3 Computational Fluid Dynamic Simulation of Pleated Filtration Devices Under Pressure

The flow rate performance of pleated filter cartridges was analyzed in several previous studies using CFD simulations.[21,33] These simulations were performed with a fixed pleat geometry, reconstructed generically or from microscopic images of filter cross sections. Pleat compressions due higher operating pressures during the filtration were not considered. Consequently, additional hydrodynamic resistances in the pleats were not considered in the previous CFD simulations and the calculated flow rates systematically overestimated experimental results. The deviations between experimental and simulated flow rates increase with rising pressure. An apparent compression factor was introduced to account for the additional pleat resistance and fit the simulated flow rate to experimental data. Yet, these simulations cannot be used as a predictive tool.

Section 5.2 describes the pleat compressions in cartridges due to the applied pressure. They correlate to mechanical properties of the spacer material. In the following, CFD simulations are used for root cause analysis to investigate the impact of pleat compressions on the hydrodynamic pleat resistance. The degrees of detail in the CFD models are systematically varied to study the individual contributions of pleat compression and reduced permeability of the nonwoven material upon compression on the total fluid flow rate. Table 3 in section 4.5 depicts a summary of the performed simulations.

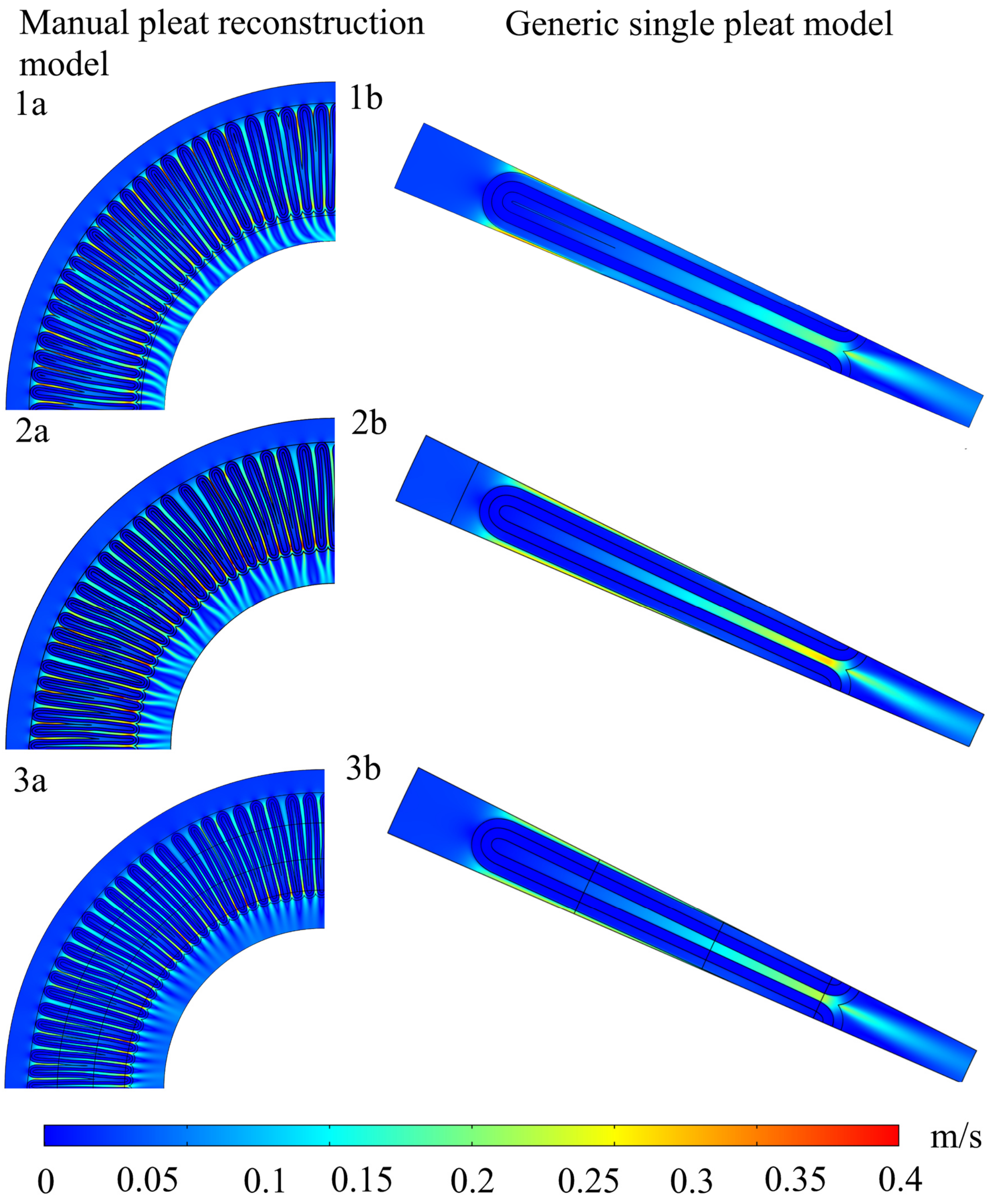

Figure 13: Simulated flow velocity profiles in 2D cross sections at a pressure drop of 1.0 bar using pleat reconstruction from CT scans (*a*) and generic single pleat design (*b*). Pleat compressions and permeability reduction neglected (*1*); pleat compressions considered but permeability neglected (*2*); pleat compressions and permeability reduction considered (*3*).

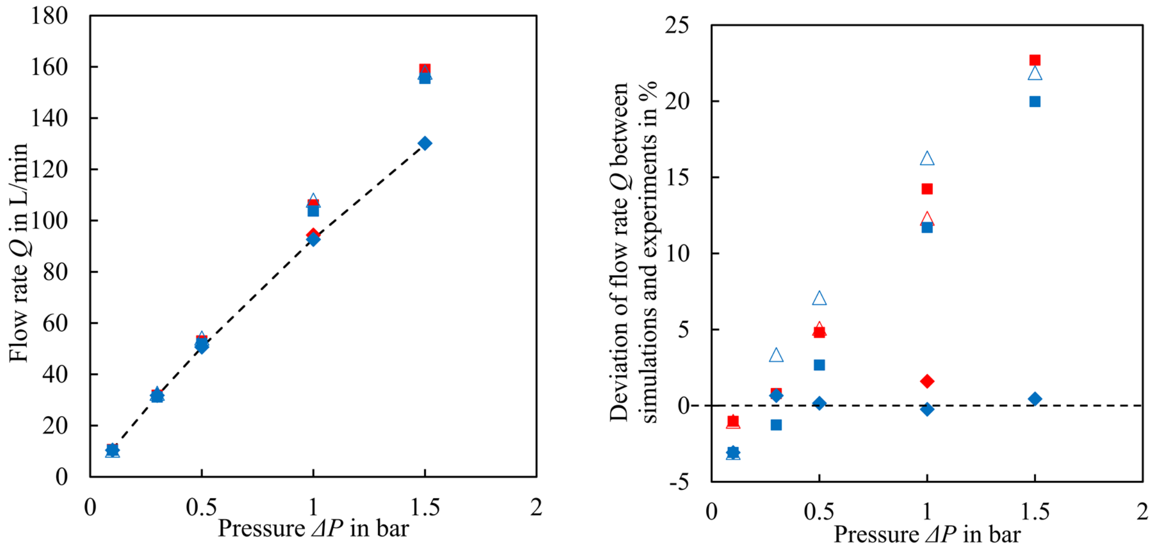

Figure 14: Calculated and experimental flow rates Q versus applied pressure ΔP *(left)* and deviations between calculated and experimental flow rates versus applied pressure *(right)*. Experimental flow rate (*black dotted line, left*); simulations 1a (*red* ■), 1b (*blue* ■), 2a (*red* Δ), 2b (*blue* Δ), 3a (*red* ◆), 3b (*blue* ◆).

Figure 13 shows the results of simulations 1a to 3b at an applied pressure of 1 bar. The simulations at different applied pressures are depicted in the supplement. Figure 14 shows the calculated flow rates of simulations 1a to 3b as well as experimentally measured flow rates of the 10” cartridges versus the applied pressure. Additionally, the graph shows the deviations between simulated and experimental flow rates versus the applied pressure.

The simulations that are based on the generic single pleat model result in similar flow rates compared with the image reconstruction model. The observed deviations are between 1.0 % and 2.5 % correspond to the findings of previous studies.[21] As shown in Figure 13, the local flow velocities in the image reconstruction model vary due to variations of the pleat widths. This is neglected in the generic single pleat model, which assumes identical thickness of all pleats. Yet these local differences of the flow velocity average out over all pleats in the cartridge. Overall, generic single pleat design is less labor-intensive than individual reconstruction of the pleat geometry from microscopic images or CT scans. Additionally, using generic pleat design, CFD simulations can be used as a predictive tool without the requirement to build prototypes.

Simulations 1a and 1b were performed without considering pleat compressions. The geometries of those simulations are taken from pleat models without applied pressure. Nonwoven permeability and porosity measured by the flow cell were used for all pressure steps (cf. supplement). Moreover, the effects of pleat compression on permeability and porosity of the nonwoven were neglected. Hence, these simulations are similar to those performed in previous studies.[21] At low differential pressure below 0.5 bar, the flow rates predicted by CFD simulations closely match the experimental results with deviations below 5 %, as shown in Figure 14. Unlike the experimental values, the simulated flow rate rises linearly as the pressure increases. Additional hydrodynamic resistance in the filter at higher operating pressures are not covered by those CFD simulations.

Simulations 2a and 2b were performed by considering pleat compression but neglecting the impact of the compression on permeability and porosity of the nonwoven. The geometry for simulation of 2a was reconstructed from the CT image at the respective pressure. Pleat widths of the generic single pleat model were obtained from the respective compression experiments of the nonwoven described in Section 4.4. The local flow velocity profiles of the simulations 2a-b deviate from those of simulation 1a-b. At the downstream side of the compressed pleats, flow velocities are locally higher in simulations 2a-b. However, the total flow rate differences in the filter cartridges between simulations 2a-b and simulations 1a-b are less than 3 % (cf. Figure 14). Additional pleat resistance at the downstream side due to a thinner pleat width is compensated by a reduced resistance due to more open pleats at the upstream side. The total hydrodynamic resistances in the pleats are equal between the simulations 1a-b and the simulations 2a-b. In conclusion, solely the altered geometry due to pleat compressions itself does not explain the additional hydrodynamic resistances during filtration at a higher pressure.

Simulations 3a and 3b consider pleat compressions as well as reduced porosity and permeability of the nonwoven due to pleat compression. The nonwoven on the downstream side of the pleats was segmented in three parts. The average porosity of each part was calculated using Equation (12) and the corresponding permeability was calculated based on Equation (14) using the mean pleat width of the respective segment.

Figure 15 depicts the calculated permeability versus the compression of nonwoven D that is incorporated in the simulated cartridge. At a nonwoven compression of 0.44, the resulting permeability on the downstream side declines from $2.45 \cdot 10^{-10}$ m² to $3.6 \cdot 10^{-11}$ m². Such a compression is observed at an operating pressure of 1 bar. Unlike the previous simulations, the flow rate well matches the experimental data with deviations below 4 %, independently of the applied pressure (Figure 14). As shown in Figure 13, the local flow rate in the pleats at 1 bar differential pressure, especially at the outlet of each pleat, is significantly higher than the flow rate in the membrane. In conclusion, the additional pleat resistance during filtration at higher pressures are caused by the reduced permeability and porosity of the nonwoven on the downstream side which in turn are caused by pleat compression. Although the permeability of the compressed nonwoven is almost two magnitudes higher than the membrane permeability of $9.65 \cdot 10^{-13}$ m², it has a significant influence on the flow rate of the filter cartridge as the flow path through this material is much longer. Further investigations are planned to analyze the impact of local flow rate on the shear rate.

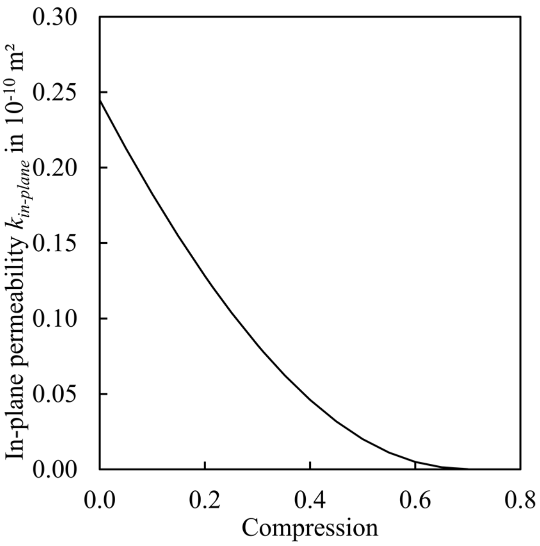

Figure 15: In-plane permeability $k_{in\text{-}plane}$ of the nonwoven as function of compression according to the Happel-p model; cf. Equation (14).

In summary, root cause analysis using CFD simulations has revealed the major factors impacting the flow rate of filter cartridges. One major factor is membrane permeability. At low differential pressures, the flow rate can be calculated appropriately by CFD simulations based on the membrane permeability and the pleat geometry. Yet at higher operating pressure, the pleats deform towards the downstream side. The pleat compression itself does not cause any significant additional hydrodynamic resistance. However, the subsequent compression of the nonwoven results in reduced porosity and permeability. When considering these additional resistances, an accurate prediction of the experimental flow rate is achieved by CFD simulations at higher pressure.

6. Conclusions

The pleat geometry has a major impact on the flow rate of pleated filter elements such as cartridges or capsules. By increasing the pleat density, a larger membrane area is packed into filter elements without changing their outer dimensions and, consequently, their footprint. This results in higher total filter throughput before the filter elements are blocked, but despite larger total membrane area, the flow rate might be reduced compared to equivalent filter elements with lower pleat density. Previous studies showed that a high pleat packing density can lower the permeability due to an additional hydrodynamic pleat resistance.[2,8,9]

This study quantitatively investigated the impact of individual parameters on the pleat resistance and the correspondingly reduced flow rate. An empirical model was developed to approximate the flow rate in 10” filter cartridges as a function of membrane permeability, membrane area incorporated, applied pressure and liquid viscosity. The total filter resistance can be split into membrane resistance or membrane permeability and pleat resistance. Membrane permeability and liquid viscosity do not significantly influence the pleat resistance. However, as more membrane area is incorporated in a filter, the pleat resistance will increase disproportionately. In addition, as the differential pressure increases, so will the pleat resistance. With 1 m² of membrane area incorporated in a filter and at a differential pressure of 1.5 bar, the pleat resistance contributes as much as 60 % to the total filter resistance. As a result, the permeability is more than halved compared with an equivalent flat disc membrane filter. The total flow rate of the 10” filter cartridge mainly depends on the membrane resistance and the pleat resistance. In cartridges with low incorporated membrane area the membrane resistance dominates the total fluid flow. Hence, the total filter flow rate in 10” cartridges rises with increasing membrane area. Yet at higher pleat packing densities, the pleat resistances become dominant and the total fluid flow rate decreases with further increase of the incorporated membrane area.

CT scans of filter capsules with a transmembrane pressure applied show significant pleat compression as the transmembrane pressure increases. The individual membrane pleats compress the nonwoven at the downstream side up to 50 % at a pressure of 1.5 bar. This pleat compression is correlated to the mechanical properties of the nonwoven material. Consequently, pleat compressions in filter cartridges were predicted based on the results of mechanical compression experiments of the nonwoven.

Finally, several CFD simulations were performed with increasing degrees of detail regarding modeling of the pleat geometry to investigate the root cause of the additional pleat resistance observed. A generic single pleat design yields results similar to those of more labor-intensive reconstruction by microscopic images or CT scans. Moreover, the geometric change due to pleat compressions itself does not to cause additional resistances but the reduced permeability and porosity of the nonwoven. The Happel-p model was used to predict the permeability of the nonwoven as a function of its compression. By using the reduced permeability and porosity of the nonwoven in the CFD model, the flow rate can be accurately predicted for a wide range of operating pressures with an error below 5 % compared to experimental data.

The findings of this study support the development of improved filter design both in academia and in industry. The CFD simulation tool developed can be used to predictively calculate the flow rate and computationally develop filter devices that incorporate soft materials that deform under pressure.

7. Acknowledgement

The authors would like to thank Mario Strauss from the Sartorius product development team for the support during manufacturing and measurement of the prototype filter cartridges as well as Zoeanne Poore-Dielschneider for proofreading the manuscript.

References

(1) Aldington, S.; Bonnerjea, J. Scale-up of monoclonal antibody purification processes. *Journal of chromatography. B, Analytical technologies in the biomedical and life sciences* **2007**, *848* (1), 64–78. DOI: 10.1016/j.jchromb.2006.11.032.

(2) Brown, A. I.; Levison, P.; Titchener-Hooker, N. J.; Lye, G. J. Membrane pleating effects in 0.2μm rated microfiltration cartridges. *Journal of Membrane Science* **2009**, *341* (1-2), 76–83. DOI: 10.1016/j.memsci.2009.05.044.

(3) Sartorius Stedim Biotech GmbH. *Sartopore® Platinum, Puplication SPK2157-e160601 datasheet*.

(4) Giglia, S.; Liu, S.; Sylvia, R. Scaling considerations to maximize the high-area advantage. *BioProcess International* **2017**, *15*.

(5) Giglia, S. *Scale-up of High Area Filters for Microfiltration of Biological Fluids*:*Points to consider for reliable scale-up*.

(6) Lutz, H. Rationally defined safety factors for filter sizing. *Journal of Membrane Science* **2009**, *341* (1-2), 268–278. DOI: 10.1016/j.memsci.2009.06.015.

(7) Dippel, J.; Handt, S.; Hansmann, B.; Loewe, T. Scalability of Sterilizing-Grade Filters in Different Filtration Modes. *PDA journal of pharmaceutical science and technology* **2020**, *74* (6). DOI: 10.5731/pdajpst.2019.011254.

(8) Kumar, A.; Martin, J.; Kuriyel, R. Scale-up of sterilizing-grade membrane filters from discs to pleated cartridges:Effects of operating parameters and solution properties. *PDA journal of pharmaceutical science and technology* **2015**, *69* (1), 74–87.

(9) Brown, A. I.; Titchener‐Hooker, N. J.; Lye, G. J. Scale‐down prediction of industrial scale pleated membrane cartridge performance. *Biotechnology and bioengineering* **2011**, *108* (4), 830–838.

(10) Chen, D.-R.; Pui, D. Y. H.; Liu, B. Y. H. Optimization of pleated filter designs using a finite-element numerical model. *Aerosol Science and Technology* **1995**, *23* (4), 579–590.

(11) Yu, H. H.; Gdulding, C. H., Eds. *Optimized ultra high efficiency filter for high-efficiency industrial combustion turbines*; American Society of Mechanical Engineers, 1992.

(12) Fotovati, S.; Tafreshi, H. V.; Pourdeyhimi, B. A macroscale model for simulating pressure drop and collection efficiency of pleated filters over time. *Separation and Purification Technology* **2012**, *98*, 344–355.

(13) Am Saleh; Hosseini, S. A.; Tafreshi, H. V.; Pourdeyhimi, B. 3-D microscale simulation of dust-loading in thin flat-sheet filters: a comparison with 1-D macroscale simulations. *Chemical Engineering Science* **2013**, *99*, 284–291.

(14) Caesar, T.; Schroth, T. The influence of pleat geometry on the pressure drop in deep-pleated cassette filters. *Filtration & Separation* **2002**, *39* (9), 48–54.

(15) Chen, X.; Papathanasiou, T. D. The transverse permeability of disordered fiber arrays: a statistical correlation in terms of the mean nearest interfiber spacing. *Transport in Porous Media* **2008**, *71* (2), 233–251.

(16) Am Saleh; Tafreshi, H. V.; Pourdeyhimi, B. Service life of circular pleated filters vs. that of their flat counterpart. *Separation and Purification Technology* **2015**, *156*, 881–888.

(17) Subrenat, A.; Bellettre, J.; Le Cloirec, P. 3-D numerical simulations of flows in a cylindrical pleated filter packed with activated carbon cloth. *Chemical Engineering Science* **2003**, *58* (22), 4965–4973.

(18) Waghode, A. N.; Hanspal, N. S.; Wakeman, R. J.; Nassehi, V. Numerical analysis of medium compression and losses in filtration area in pleated membrane cartridge filters. *Chemical Engineering Communications* **2007**, *194* (8), 1053–1064.

(19) Nassehi, V.; Hanspal, N. S.; Waghode, A. N.; Ruziwa, W. R.; Wakeman, R. J. Finite-element modelling of combined free/porous flow regimes:Simulation of flow through pleated cartridge filters. *Chemical Engineering Science* **2005**, *60* (4), 995–1006.

(20) Giglia, S.; Rautio, K.; Kazan, G.; Backes, K.; Blanchard, M.; Caulmare, J. Improving the accuracy of scaling from discs to cartridges for dead end microfiltration of biological fluids. *Journal of Membrane Science* **2010**, *365* (1-2), 347–355. DOI: 10.1016/j.memsci.2010.09.032.

(21) Eirini Velali; Jannik Dippel; Birgit Stute; Sebastian Handt; Thomas Loewe; von Lieres. Model-based performance analysis of pleated filters with non-woven layers. *Separation and Purification Technology* **2020**, *250*, 117006.

(22) Terminology for membranes and membrane processes (IUPAC Recommendation 1996). *Journal of Membrane Science* **1996**, *120* (2), 149–159.

(23) Tahir, M. A.; Tafreshi, H. V. Influence of fiber orientation on the transverse permeability of fibrous media. *Physics of Fluids* **2009**, *21* (8), 83604. DOI: 10.1063/1.3211192.

(24) Eriksson, L.; Johansson, E.; Kettaneh-Wold, N.; Wikström, C.; Wold, S. Design of experiments. *Principles and Applications, Learn ways AB, Stockholm* **2000**.

(25) Jornitz, M. W.; Meltzer, T. H. *Filtration handbook: integrity testing*; PDA, 2003.

(26) Schröder, W. *Fluidmechanik*; Mainz, 1999.

(27) Jaganathan, S.; Tafreshi, H. V.; Pourdeyhimi, B. A realistic approach for modeling permeability of fibrous media: 3-D imaging coupled with CFD simulation. *Chemical Engineering Science* **2008**, *63* (1), 244–252.

(28) Chen, X.; Papathanasiou, T. D. On the variability of the Kozeny constant for saturated flow across unidirectional disordered fiber arrays. *Composites Part A: Applied Science and Manufacturing* **2006**, *37* (6), 836–846.

(29) Mao, N.; Russell, S. J. Directional Permeability in Homogeneous Nonwoven Structures Part II: Permeability in Idealised Structures. *The Journal of The Textile Institute* **2000**, *91* (2), 244–258.

(30) Rawal, A. A cross-plane permeability model for needle-punched nonwoven structures. *The Journal of The Textile Institute* **2006**, *97* (6), 527–532.

(31) Håkanson, J. M.; Toll, S.; Lundström, T. S. Liquid permeability of an anisotropic fiber web. *Textile research journal* **2005**, *75* (4), 304–311.

(32) Lawrence, C. A.; Shen, X. An Investigation into the Hydraulic Properties of Needle-punched Nonwovens for Application in Wet-press Concrete Casting Part II: Predictive Models for the Water Permeability of Needle-punched Nonwoven Fabrics. *The Journal of The Textile Institute* **2000**, *91* (1), 61–77.

(33) Wakeman, R. J.; Hanspal, N. S.; Waghode, A. N.; Nassehi, V. Analysis of pleat crowding and medium compression in pleated cartridge filters. *Chemical Engineering Research and Design* **2005**, *83* (10), 1246–1255.